Earth and Planetary Science Letters 515 (2019) 200–208

Contents lists available at ScienceDirect

Earth and Planetary Science Letters

www.elsevier.com/locate/epsl

The impact of spatially-variable basal properties on outlet glacier flow

Stephen Koellner [a], Byron R. Parizek [b,c,*], Richard B. Alley [c], Atsuhiro Muto [d], Nicholas Holschuh [e]

[a] Department of Mathematics, The Pennsylvania State University, University Park, PA 16802, USA
[b] Mathematics and Geoscience, The Pennsylvania State University, DuBois, PA 15801, USA
[c] Department of Geosciences and Earth and Environmental Systems Institute, The Pennsylvania State University, University Park, PA 16802, USA
[d] Department of Earth and Environmental Science, Temple University, Philadelphia, PA 19122, USA
[e] Department of Earth and Space Sciences, University of Washington, Seattle, WA 98195, USA

ARTICLE INFO

Article history:
Received 7 September 2018
Received in revised form 15 March 2019
Accepted 17 March 2019
Available online 2 April 2019
Editor: M. Ishii

Keywords:
basal rheology
basal topography
outlet glacier
grounding line
ice-ocean interactions

ABSTRACT

The spatially variable basal flow law suggested by geophysical data from Thwaites Glacier, West Antarctica produces modeled ice-flow response to warming that differs notably from the response of commonly assumed spatially uniform flow laws, with implications for future sea-level rise. Unlike many ice-sheet outlets, Thwaites flows across rather than along prominent topography, with hard stoss faces where form drag is understood to give a low-stress-exponent basal flow law and soft lee-side tills likely to give nearly-plastic behavior. Applying the PSU 2-D higher-order flowline model to a range of idealized Thwaites-like topographies, we test the impact of nearly plastic, nearly viscous, and spatially variable basal rheology on forced grounding-line evolution.

In agreement with previous findings, for spatially uniform basal rheology, the timing and rate of grounding-line retreat depend strongly on the bed exponent, with plastic rheology promoting longer stability at the current grounding line but faster retreat once destabilized. Additionally, we find that retreat over mixed-rheology beds is sensitive to the wavelength of the basal topography. For outlet-glacier flow across long-wavelength bumps ($\gtrsim$10 km), behavior falls between that for uniform viscous and plastic beds, yet closer to plastic. However, over shorter-wavelength topography, at times, grounding-line retreat is slower than for either uniform-rheology end-member. Accurately accounting for variable basal conditions in ice-sheet models thus is critical for improving projections of both the timing and magnitude of retreat.

1. Introduction

Ice-ocean interactions can drive grounding-line evolution for Antarctica's rapidly changing marine-terminating outlet glaciers (Rignot, 1998; Rignot et al., 2014). An accurate physical understanding of the spatiotemporal dynamic inland responses to ice-front forcings is critical for reliable projections of global sea-level rise (Stocker et al., 2013). For example, whether and how physical processes are represented within ice-sheet models has led to a wide range (0.08-1 m) of estimated sea-level contributions from Antarctica this century (Bindschadler et al., 2013; Golledge et al., 2015; Ritz et al., 2015; DeConto and Pollard, 2016).

There is evidence for the near total collapse of the West Antarctic Ice Sheet (WAIS), as was first suggested by Mercer (1968), although the time(s) and rate(s) of shrinkage are not known well (reviewed by Alley et al., 2015). As pointed out by Hughes (1981), the Amundsen Sea Embayment (ASE) is a dynamically influential region for WAIS as a whole, with the steep, submarine retrograde beds of ASE favoring the marine ice sheet instability (MISI; Weertman, 1974; Schoof, 2007). ASE contains enough ice to raise sea level more than 1 m, connected through deep basins to a reservoir with the potential to raise sea level more than 3 m (Bamber et al., 2009). Discharge from ASE increased 77% between 1973 and 2013 (Mouginot et al., 2014). Increased ice-shelf basal melting in response to warmer ocean water circulating in ice-shelf cavities (Jacobs et al., 1996; Payne et al., 2004; Jenkins et al., 2010; Jacobs et al., 2011; Dutrieux et al., 2014) is leading to accelerated outlet-glacier thinning and rapid grounding-line retreat (Rignot, 1998; Rignot et al., 2014; Christianson et al., 2016), indicating that future instability of this marine sector is likely and might have al-

* Corresponding author at: Mathematics and Geoscience, The Pennsylvania State University, DuBois, PA 15801, USA.
E-mail address: parizek@psu.edu (Parizek).

https://doi.org/10.1016/j.epsl.2019.03.026

ready been triggered (Pritchard et al., 2012; Mouginot et al., 2014; Joughin et al., 2014; Rignot et al., 2014).

Particular interest is focused on ASE's Thwaites Glacier (TG) because it is not confined in a narrow bedrock channel or by a large buttressing ice shelf, it has a retrograde bed that dynamically connects it to the rest of WAIS, and it has a faster-than-average ice velocity when compared to other Antarctic ice streams (Pfeffer et al., 2008). The mass balance of TG has become increasingly negative since 1996, and the increased mass loss is one of the driving factors behind the acceleration of ice loss from West Antarctica as a whole (Harig and Simons, 2015).

Prior modeling has shown the importance of basal topography and the basal flow law in controlling stability. Topography is linked to threshold behavior at TG and other marine-ending glaciers, with the grounding line exhibiting long-term stability on one basal high, and then migrating rapidly to the next high during both retreat and advance (Wellner et al., 2006; Alley et al., 2007; Joughin et al., 2010; Parizek et al., 2010). Such topographic effects interact with bed rheology. Simulations for TG by Parizek et al. (2013), for example, found conditions under which the grounding line remained stable on its topographic high despite ocean warming for an effectively plastic bed, but retreated in response to the same forcing with a viscous bed.

TG and neighboring Pine Island Glacier and their catchment areas flow over heterogeneous beds (Joughin et al., 2009; Schroeder et al., 2014). Of particular interest here, seismic surveying of an upstream reach of TG found a long, relatively flat region with soft till, upstream of rough subglacial highlands with relatively hard stoss faces (those for which the bed rises in the direction of ice flow) and soft till on lee sides (bed drops in elevation in the direction of ice flow) (Muto et al., 2019).

Glacial flow over soft till is best described by a plastic or nearly plastic basal flow law (Tulaczyk et al., 2000; Rathbun et al., 2008; Walker et al., 2014), whereas the flow law for hard till or bedrock depends on a number of factors including bed roughness, ice debris concentration, and the hydrologic system (Paterson, 1994). Provided the shear stress remains below the maximum that can be supported by the bed (Iken, 1981; Schoof, 2005), however, hard regions are generally modeled with viscous or low-stress-exponent behavior (Weertman, 1957). Together with the observations of (Muto et al., 2019), this suggests that the basal flow law varies along flow on TG, in a way correlated with topography.

Here we use a numerical ice-flow model to assess whether and how a spatially-variable basal flow law and/or topographic variability influence the nature of retreat, and thereby impact the rate and magnitude of sea-level rise. We use a simplified model with idealized geometry so that we can explore a wide range of parameter space, to learn whether this level of basal complexity affects outlet-glacier stability in comparison to a bed with a uniform flow law. We find some conditions under which the behavior of the spatially variable bed falls outside the behavior exhibited by nearly viscous and nearly plastic beds. This suggests that accurate models of TG will require accurate specification of both basal topography and basal flow law, with implications for the design of field programs as well as modeling.

2. Model

The PSU (Penn State University) two-dimensional (in along-flow, x, and vertical, z, Cartesian coordinates), higher-order, finite element model (Parizek et al., 2010) originally followed most models in assuming an along-flow homogeneous basal rheology. Here, we briefly review the model, and then describe the modifications and the domain for this study (refer to Parizek et al., 2010, 2013 for a more detailed description).

2.1. Ice-flow

The ice-flow model assumes a power law rheology for ice, $n = 3$ (Glen, 1955), with deviatoric-stress (σ'_{ij}) proportional to effective viscosity (ν) and strain-rate ($\dot{\varepsilon}_{ij}$):

$$\sigma'_{ij} = 2\nu\dot{\varepsilon}_{ij} \tag{1}$$

$$\nu \equiv \frac{B}{2}\dot{\varepsilon}_*^{\frac{1-n}{n}} \tag{2}$$

In turn, the effective viscosity (Eq. 2) depends on both an ice-hardness parameter (B) and the effective strain-rate ($\dot{\varepsilon}_*$). Temperature-dependent values for B are computed from Table 5.2 in Paterson (1994), given $B = A^{-1/n}$, where A is the ice-softness parameter. Ice temperature is assumed to change linearly with depth from the surface temperature down to the pressure melting point at the base of the ice.

Mass balance is width- and depth-averaged, with an assigned basal-melting rate, $\dot{B}$, that is non-zero only along floating ice and is variable in time. We used basal melting rates between 20 m/yr and 100 m/yr, within the observed range for Amundsen Sea ice shelves (Shean et al., 2018) but set large enough to force a substantial retreat along our idealized domain, in order to help interpret and distinguish between the dynamic impact of basal rheology and topography during retreat. Surface accumulation is set to 0.13 m/yr across the domain and held constant. We apply a constant-ice-flux upstream boundary condition. Flow is fast enough that ice flux in grounded regions is dominated by this upstream flux, and small changes in surface accumulation or basal melting beneath grounded ice would not affect the results; the melting beneath floating ice does have significant effects. For the downstream boundary condition, we apply a 15-m minimum-thickness when the ice front is within the domain, and a free-radiation condition when the ice front is at the end of the domain. The flowband width, β, is held fixed at 50 km throughout all simulations.

Horizontal momentum balance follows:

$$\frac{\partial}{\partial x}\left(2\nu\left(2\frac{\partial u}{\partial x} + \frac{u}{\beta}\frac{\partial \beta}{\partial x}\right)\right) + \frac{\partial}{\partial z}\left(\nu\frac{\partial u}{\partial z}\right) = \rho g\frac{\partial (s-z)}{\partial x} + \frac{2}{\beta}\tau_s \tag{3}$$

with along-flow ice velocity, u, ice density, ρ, acceleration due to gravity, g, and ice surface elevation, s. Side friction, τ_s, is variable both horizontally (along flow) and vertically and is parameterized assuming it acts within a narrow lateral shear zone (Dupont and Alley, 2005; Goldberg et al., 2009; Parizek et al., 2010). If the ice-shelf extends outside of the model domain ($x > 160$ km), it is assumed to provide no extra buttressing to the outlet glacier; otherwise, stress-free and hydrostatic ice-front conditions are applied above and below sea level, respectively.

2.2. Basal drag

Assuming that deformation within a thin basal boundary layer is dominated by vertical shear, basal rheology is represented by:

$$\tau_b = B_b u(b)^{\frac{1}{m}} \tag{4}$$

where τ_b and B_b are the drag and basal friction coefficient, respectively, at the basal interface ($z = b$). The bed exponent, m, is either held constant across the domain, as is customary in ice-sheet modeling, or is assigned a spatially-variable power, which specifies the width-averaged basal rheology along the flowline. The main rheologies tested are linear-viscous ($m = 1$), weakly non-linear ($m = 3$, used in our Control Runs; see Section 3), effectively plastic ($m = 8$, chosen following Rathbun et al. (2008)), and a mixed-bed, with regions of $m = 3$ and $m = 8$. A linear-viscous bed ($m = 1$) has often been used in models, and arguably is the lowest physically likely value, arising from regelation around bedrock obstacles

Table 1
Simulations and their descriptions. Run Suites progress from ice flow over (A) a planar, retrograde bed, through inclusion of superimposed 100-m-amplitude topographic variability with decreasing wavelength of (B) 60 km, (C) 10 km, and (D) 8 km, respectively. The Control Runs for the primed Suites (B' and D') include a sinusoidally varying basal friction field, such that up- (down-) sloping points of inflection on the bed have a maximum (minimum) friction coefficient, while maintaining comparable surface speeds and profiles to the steady state B and D runs, respectively. Asterisk Suites (C* and D*) eliminate basal melting within upstream-shelf regions that form during retreat. Note that all basal rheologies ($m = 1, 8$, and $8 \leftrightarrow 3$) are placed on the 'Tested Bed' for each Run Suite.

Run suite	Control run	Tested bed	Ocean forcing
A	$m = 3$ B_b constant	Planar bed	$\dot{B} = 20$ m/yr $\rightarrow$ 60 m/yr; $B_s = 0.5 \cdot B_{s_o}$ (175 years)
B	$m = 3$ B_b constant	Bumpy bed ($\lambda = 60$ km)	$\dot{B} = 20$ m/yr $\rightarrow$ 100 m/yr; $B_s = 0.25 \cdot B_{s_o}$ (80 years)
C	$m = 3$ B_b constant	Bumpy bed ($\lambda = 60 \rightarrow 10$ km)	$\dot{B} = 20$ m/yr $\rightarrow$ 100 m/yr; $B_s = 0.25 \cdot B_{s_o}$ (80 years)
D	$m = 3$ B_b constant	Bumpy bed ($\lambda = 60 \rightarrow 8$ km)	$\dot{B} = 20$ m/yr $\rightarrow$ 100 m/yr; $B_s = 0.25 \cdot B_{s_o}$ (80 years)
C*	$m = 3$ B_b constant	Bumpy bed ($\lambda = 60 \rightarrow 10$ km)	$\dot{B} = 20$ m/yr $\rightarrow$ 100 m/yr; $B_s = 0.25 \cdot B_{s_o}$ (80 years); melt only along main shelf
D*	$m = 3$ B_b constant	Bumpy bed ($\lambda = 60 \rightarrow 8$ km)	$\dot{B} = 20$ m/yr $\rightarrow$ 100 m/yr; $B_s = 0.25 \cdot B_{s_o}$ (80 years); melt only along main shelf
B'	$m = 3$ B_b sinusoidal	Bumpy bed ($\lambda = 60$ km)	$\dot{B} = 20$ m/yr $\rightarrow$ 100 m/yr; $B_s = 0.25 \cdot B_{s_o}$ (80 years)
D'	$m = 3$ B_b sinusoidal	Bumpy bed ($\lambda = 60 \rightarrow 8$ km)	$\dot{B} = 20$ m/yr $\rightarrow$ 100 m/yr; $B_s = 0.25 \cdot B_{s_o}$ (80 years)

(Weertman, 1957) or in other ways. Values higher than $m = 8$ could occur under some circumstances (e.g., Tulaczyk et al., 2000; Rathbun et al., 2008), but we find that $m = 8$ captures much of the nonlinearity while maintaining numerical stability across large simulation suites, including those with prescribed mixed-rheology beds. We choose the intermediate $m = 3$ as a possible value for motion over a rough bed enabled primarily by enhanced creep around large bedrock obstacles (Weertman, 1957). Beds with $m = 2$ might occur (Weertman, 1957), and other values are possible and could be explored in future studies, but we believe these provide good sampling of likely behavior.

3. Simulations

Each Suite of experiments (Table 1) was initialized and run to steady state through 2500 simulated years of constant forcing, followed by between 80 and 100 years of ocean forcings (enhanced basal-melting and reduced lateral drag) to test the impact of basal properties on outlet-glacier retreat. The bedrock profiles are changed, progressing from Run Suite A through D (Section 3.1).

In some runs, the forced retreat causes the ice to thin sufficiently to float in the ocean for grid boxes upstream of ice that remains grounded on a bedrock high. We simulate end-member cases of zero melting of the ice above such upstream-shelf regions (experiment Suites labeled with asterisks), and melting above them at the full ice-shelf rate (non-asterisk Suites).

Each Suite has a Control Run, which is used to initialize other runs in the Suite (Section 3.2). Most Control Runs use a spatially constant basal friction coefficient. For Suites indicated with a prime, however, the basal friction coefficient varies with the sinusoidal basal morphology to simulate the harder stoss-side and softer lee-side conditions indicated by seismic data (Muto et al., 2019), thereby using a traditional constant-rheology approach to simulating variable basal conditions.

3.1. Bedrock profile

We test four different bedrock topographies, b_r, one planar (Run Suite A, Table 1; see Supplemental Fig. S1.):

$$b_r = -1200 + 0.003x \tag{5}$$

and three 'bumpy' (Run Suites B-D), all of which are retrograde with a background slope akin to TG (see Fig. 9 from Parizek et al., 2013). Because the purpose of this study is to isolate how variable basal conditions influence grounding-line retreat forced by reduction of ice-shelf buttressing, these idealized beds were not intended to exactly match the bedrock profile data from TG (cf. Parizek et al., 2013). Instead, for the purpose of comparison, they were designed to be similar in general character and wavelength to the lower ~160 km of TG.

To simulate the ~100-m amplitude ridge and valley structure, a 'bumpy' bed is generated by rotating the following sine function with wavelength, λ:

$$b_{ro} = -100 \cdot sin\left(\frac{2\pi}{\lambda}x\right) \tag{6}$$

by the same grade as the 'planar' bed:

$$b_r = -1200 + 0.003 \cdot b_{ro} \tag{7}$$

The three different λ-dependent 'bumpy' topographies include: i) constant $\lambda = 60$-km (Run Suites B and B'; see inset profiles in Figs. 2, S2) and λ varying linearly from 60 km at the upstream end down to either ii) 10-km (Run Suites C and C*; see Supplemental Fig. S3) or iii) 8-km (Run Suites D, D*, D') over the first 50 km, then held constant at these shorter wavelengths to the end of the domain (Fig. 1).

3.2. Control runs

Prior work shows that forced outlet-glacier retreat is sensitive to both basal rheology and the initial flow state. Realistic simulations of TG or other outlet glaciers will start with known bed elevation, surface elevation and surface velocity, but perhaps with poorly known basal rheology. We thus wish to assess the influence of basal rheology on forced retreat, which requires starting all runs in a suite from the same flow state. To do this, we conduct a Control Run for each suite, allowing each Control to reach a steady

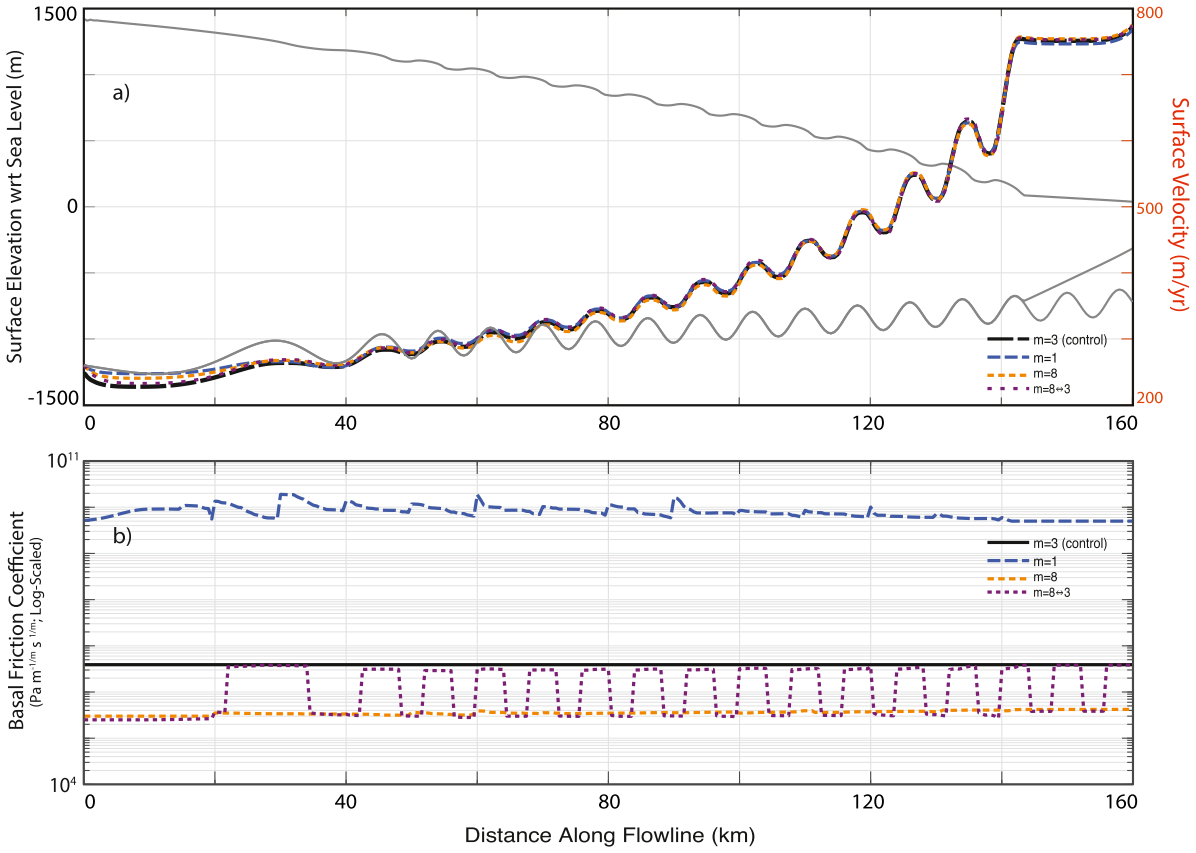

Fig. 1. Steady-state for Run Suite D Control Run. a) Using the resulting ice geometry (left ordinate axis, with ice and bed profiles displayed in thin, solid grey), b) basal-friction-coefficient fields for the various basal rheologies (shown on a semi-log plot) are tuned to reproduce the steady-state surface velocities from the $m = 3$ Control Run (panel (a), right ordinate axis, with speeds displaced as thick, dashed curves).

flow state prior to applying the ocean forcing. Given these steady-state ice profiles, we then tune the basal friction coefficient for other runs in the suite to match the steady-state surface-velocity distribution over the specified bed of the Control Run.

Unless otherwise noted, all Control Runs have a spatially constant, weakly non-linear basal rheology (with $m = 3$) and effective basal friction coefficient of $B_b = 3.9 \times 10^6$ Pa $s^{1/3}$ $m^{-1/3}$. An exception is made for the B' and D' Run Suites, in which the Control Runs include sinusoidally enhanced (diminished) B_b on the up-sloping/stoss (down-sloping/lee) regions of the bed to reflect recent seismic data from upper TG (Muto et al., 2019). Each Control Run has an initial upstream ice thickness of $h_o = 2500$ m and an initial linearly sloping surface down to the grounding line. All of the runs start with a constant upstream velocity of $u_o = 235$ m/yr, which together with h_o and β leads to the upstream flux boundary condition that is maintained throughout the simulations. Prior to forcing retreat, the side friction coefficient is held constant at $B_{s_o} = B_s = \tau_s u^{-1/3} = 3.4 \times 10^7$ Pa $s^{1/3}$ $m^{-1/3}$, which corresponds to the lateral boundaries supporting roughly 6% of the driving stress for our outlet glacier geometry and ice-flow speeds. Bedrock topography (Section 3.1), the basal friction coefficient field (Section 3.3), and the prescribed ocean forcings (Section 3.4) are varied between Control Runs (Table 1), but all other variables remain the same.

3.3. Basal rheology

The steady-state, Control Run outputs from simulations across various bedrock profiles (Section 3.1) then serve as the 'physical data' for the initialization of our simulations that test the impact of various choices of basal rheology ($m = 1, 8, 8 \leftrightarrow 3$) on outlet-glacier retreat across these four topographies. For each non-Control Run in a suite, we tune the spatial distribution of B_b to diagnostically reproduce the Control-Run surface velocities generated from the initially unforced steady-state ice geometries (e.g., Fig. 1). For the suite with mixed-bed rheology and a planar bed, we alternate the bed exponent every 30 km. Whereas, on a bumpy bed, the exponent is lower (higher) across topographic highs (lows) to reflect regelation across small obstacles or enhanced creep associated with the form drag of larger obstacles and deformation of weaker tills deposited within the lows. Again, an exception is made for the B' and D' Run Suites, in which the lower (higher) exponent is placed on the stoss (lee) sides (Figs. 4, S2), most consistent with the seismic data of Muto et al. (2019). As with the Control Runs, each of these basal-rheology simulations was allowed to reach its own, quite similar to the Control, steady-state configuration prior to forcing (see 'Steady State' profiles in Figs. 2–4).

3.4. Ocean forcings

As noted above, we use a flowline model for speed and flexibility, allowing us to explore a wide range of parameter space to isolate key processes and gain a dynamic understanding of how and why mixed-rheology beds are likely to influence the style and rate of outlet-glacier retreat across undulating topography. But, this requires parameterizing or otherwise dealing with transverse variations. This is particularly important for the ice-shelf regions that form upstream of grounded nodes during forced retreat (e.g., Joughin et al., 2014). In nature, ice above the upstream region of flotation will experience basal melt rates that depend on the extent of connectivity with the ocean. This floating ice could be a well-connected part of a sub-ice-shelf cavity

along a flowline crossing an ice rumple, a part of the sub-ice-shelf cavity with only limited connections to the main cavity, perhaps during high tides (Horgan et al., 2013), or even a region that is mostly or completely isolated from the ocean. We simulate the limiting cases, conducting some runs with full ice-shelf basal melting in these regions and other runs with zero melting applied to these regions. (Note that such regions have been termed "lakes" in some prior studies (Parizek et al., 2013; Joughin et al., 2014).) All of our simulations use relatively aggressive forcing to generate retreat; additional simulations assessing the importance of spatially variable basal rheology on weakly forced retreat could be conducted in the future.

To this end, ocean forcing is simulated through perturbations to two parameters in the model: the basal melt rate $\dot{B}$ is increased and the side friction coefficient B_s is reduced for floating regions (Joughin et al., 2008). Perturbations were chosen to be consistent with values used in other studies of TG (e.g., Joughin et al., 2014) and to generate a large response in a timely manner. For Run Suite A the forcing is not as severe ($\dot{B}$ increased from 20 to 60 m/yr and B_s decreased 50% for 100 years) because the linear sloping bed drastically reduces the stability of the grounding line and leads to complete retreat under the full forcing. For all other runs, the basal melt rate increases to $\dot{B} = 100$ m/yr and the side friction coefficient is reduced by 75% for 80 years. Furthermore, for the C* and D* run suites, basal melting occurs only on the main ice shelf and is not applied to the upstream extensions that form during retreat.

4. Results

4.1. Suite A: Planar bed

For lower m, and in agreement with prior findings (Parizek et al., 2013), thinning is more strongly localized downstream near the forcing; raising m increases thinning upstream while reducing thinning downstream. This causes the grounding line (see Supplemental Fig. S1) to retreat farthest for the linear-viscous ($m = 1$) basal rheology and least for the effectively-plastic bed ($m = 8$). The retreat rate for the linear viscous bed is nearly constant, whereas initially slower rates later accelerate with increasing bed exponent. The mixed-bed ($m = 8 \leftrightarrow 3$) rheology falls between those for the weakly non-linear ($m = 3$) and effectively-plastic beds but closer to effectively-plastic, likely due to the rapid regional transport of ice from effectively-plastic to weakly non-linear patches, thereby limiting the $m = 3$ localized drawdown.

4.2. Suite B: Bumpy bed, 60-km wavelength

Consistent with previous findings (e.g., Wellner et al., 2006; Alley et al., 2007; Joughin et al., 2010; Parizek et al., 2010), grounding-line retreat is slowed going up slopes toward topographic highs, for every choice of basal rheology (Fig. 2). Conversely, a MISI-style acceleration ensues as the grounding line races down retrograde slopes. For constant basal rheologies, thinning patterns are similar to those in Run Suite A and, once again, the grounding line retreats farthest on the linear-viscous bed and least on the effectively-plastic bed. Retreat on the mixed-rheology bed ($m = 8 \leftrightarrow 3$) initially falls between the weakly non-linear ($m = 3$) and effectively-plastic ($m = 8$) rheologies, but toward the middle of the run all of the nonlinear rheologies converge while retreating up a bedrock high, followed by faster reteat over the crest and into the next valley (model years ~55-80) in the weakly non-linear case. Although the mixed-rheology and effectively-plastic grounding lines remain close together for the rest of the run, the remaining ice at the end is thinner for the effectively-plastic bed, suggesting that it would retreat more rapidly in the future (Parizek et al., 2013).

4.3. Suite C: Bumpy bed, 60-km to 10-km wavelength

Shorter-wavelength bedrock bumps reduce the time-averaged retreat rates, with nearly-steady positions on peaks punctuated by rapid backstepping to the next bump after destabilization. Retreat is monotonic for the linear-viscous bed, but more complex for higher-exponent beds. Upstream ice thins to flotation despite persistent grounding on the bedrock high, resulting in upstream extension of the ice shelf; here, we apply ice-shelf melt rates to these regions. The stress redistribution associated with loss of basal friction in these regions causes a short-term re-advance of the position of the most seaward grounded node, before eventual ungrounding from the bump crest with the upstream extension merging into the main ice shelf. Because thinning does not spread far inland from the grounding line for the linear-viscous basal rheology, ice over the neighboring valley is too thick to thin to flotation. For constant basal rheologies, the general patterns of retreat and thinning are similar to Run Suites A (planar bed; Fig. S1) and B (60-km wavelength bed; Fig. 2), with greatest retreat on the linear-viscous bed (~60 km from steady state), least on the effectively-plastic bed (~30 km from steady state), and intermediate for the mixed-rheology bed (see Supplemental Fig. S3). For all bed exponents, grounding-line stability persists longest on the two downstream-most bumps and decreases monotonically for subsequent bump crests that are farther below sea level. This pattern of early stability and late reduction in stability for deeper ridges is pronounced for higher-exponent beds. Greater inland thinning with higher bed exponents sets the stage for their eventual, more rapid destabilization.

4.4. Suite D: Bumpy bed, 60-km to 8-km wavelength

Reducing the spacing of the downglacier 100-m-amplitude bumps from 10 km (Suite C) to 8 km (Suite D) causes the linear-viscous rheology to join the others in developing upstream ice-shelf extensions during retreat (Fig. 3). The patterns of thinning remain consistent with our previous modeling results. For higher bed exponents, the greater upstream thinning and therefore greater decrease in time spent by the grounding line on inland topographic highs is now strong enough that the $m = 8$ grounding line eventually pulls back farther (~60 km) than both the weakly non-linear and linear-viscous rheology runs (~50 km). Unlike outputs from the previous Suites, the mixed basal rheology retreats least (~34-km retreat from its steady-state position).

4.5. Suites C* and D*: Bumpy bed with laterally continuous ridges

As expected, eliminating melting above upstream ice-shelf extensions increases the duration of grounding-line stability on basal highs and decreases the distances of maximum retreat for all beds and rheologies that produce such extensions (see Figs. 3, S3). The stabilizing effect of eliminating ocean melt from these upstream extensions is most pronounced for the effectively plastic bed and least pronounced for the linear-viscous (Suite D*) and mixed-rheology (Suite C*; when neglecting linear-viscous due to the lack of upstream-extension development) beds.

4.6. Suites B' and D': Bumpy bed with control following stoss-/lee-side conditions

Introducing a sinusoidally varying friction coefficient for the Control Runs, with greatest lubrication halfway down lee faces and least lubrication halfway up stoss faces, causes slight changes in the steady-state surface topography when compared to a constant B_b field. The location where driving stress naturally peaks due to form drag as ice flows over the bumps is shifted slightly upglacier,

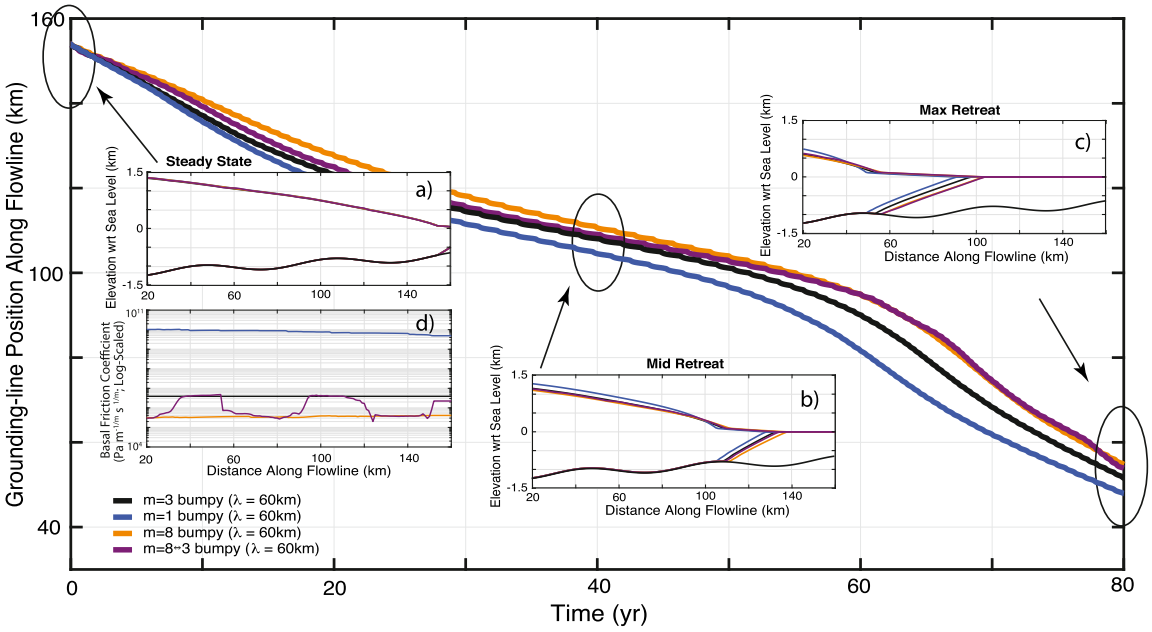

Fig. 2. Grounding-line evolution and outlet-glacier profiles for Run Suite B. The location of the last grounded node along the flowline transect as a function of time since the onset of the ocean-forcing perturbation is shown for each basal rheology tested, with the black curve representing the Control Run with a weakly non-linear basal rheology ($m = 3$), blue for the linear-viscous bed ($m = 1$), orange for effectively plastic ($m = 8$), and purple for mixed rheology ($m = 8 \leftrightarrow 3$). Inset panels a)-c) display the outlet-glacier profiles corresponding to the circled time periods (0, 40, and 80 simulated years after the onset of the ocean-forcing perturbation) for each basal rheology, with $m = 3$ and the bedrock profiles displayed in black and other ice-profile colors as above. The characteristic impacts of basal rheology and topography on localized versus regional drawdown and retreat rates are evident, as discussed in the text. Inset panel d), basal-friction-coefficient fields for the various basal rheologies (shown on a semi-log plot).

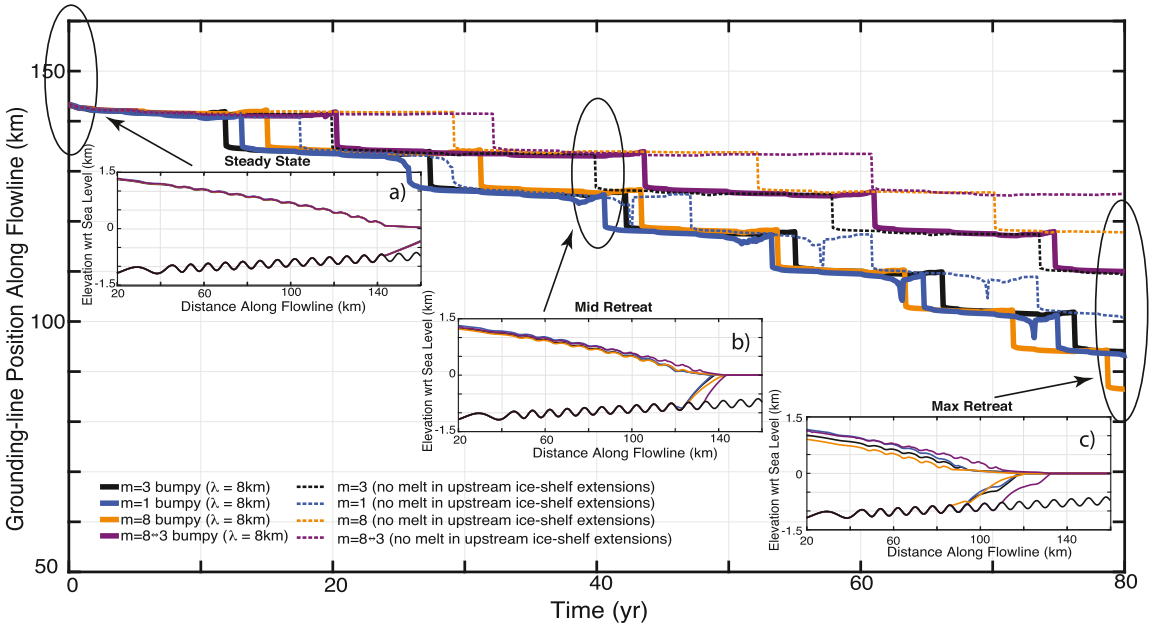

Fig. 3. Grounding-line evolution and profiles for Run Suites D and D*, with basal rheologies ranging from linear viscous to effectively plastic. Solid lines depicting Run Suite D grounding-line evolution as in Fig. 2, with dashed lines associated with retreat histories when oceanic forcing is blocked from the upstream ice-shelf extensions (Run Suite D*). Inset panels a)-c) display the outlet-glacier profiles corresponding to the circled time periods (0, 40, and 80 simulated years after the onset of the ocean-forcing perturbation) for each basal rheology, with $m = 3$ and the bedrock profiles displayed in black and other ice-profile colors as in Fig. 2.

with an increase in ice thickness occurring over valleys and down-sloping sections of neighboring bumps to compensate for the increase in basal drag on the up-sloping regions. These changes in ice thickness become more pronounced with shorter wavelength bedrock topography (cf. Run Suites B' and D').

For Run Suite B' (longer wavelength bed; see Supplemental Fig. S2), introducing the sinusoidal basal friction field slightly delays grounding-line retreat for every basal rheology tested. When compared to the constant-rheology B-suite runs, the B' grounding-line positions are a bit more stable on both stoss and lee sides of the bedrock, with extra drag on the stoss side slowing the MISI-style retreat and the extra thickness over the valleys and lee sides compensating the reduced drag there. With mixed basal rheology, stability over the effectively-plastic lee regions is slightly reduced while stability increases across the weakly non-linear stoss regions of the bed. This behavior arises as ice is transported more rapidly with lower surface slopes/driving stresses across the weak bed and into stronger-bed regions, where it delays the localized drawdown

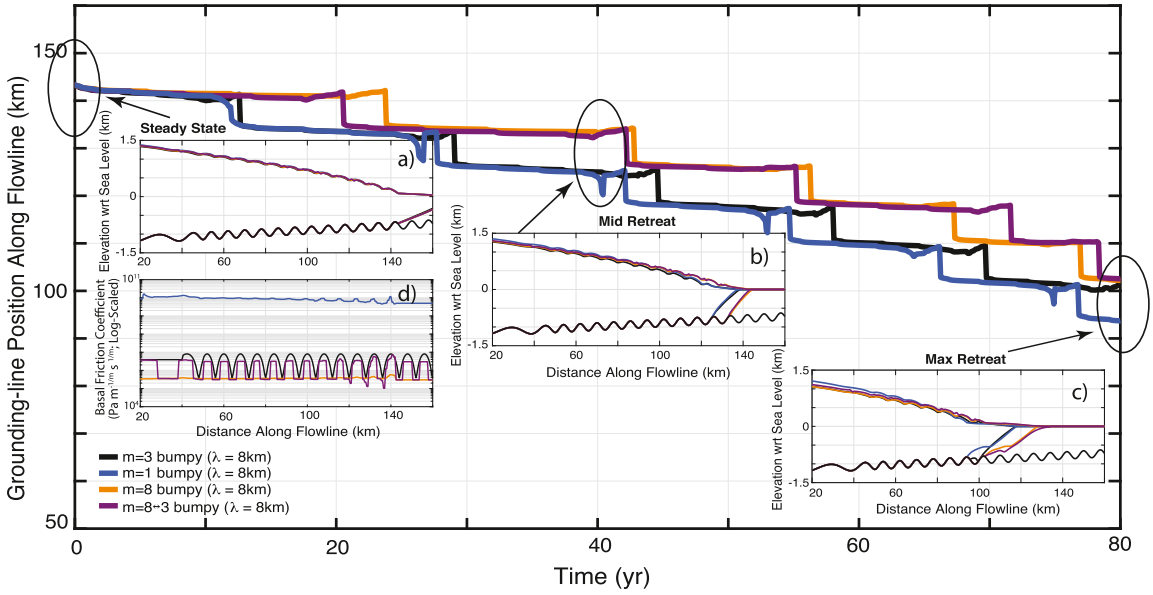

Fig. 4. Grounding-line evolution and profiles for Run Suite D', with basal rheologies ranging from linear viscous to effectively plastic. Solid lines depicting Run Suite D' grounding-line evolution as in Fig. 2. Inset panels a)-c) display the outlet-glacier profiles corresponding to the circled time periods (0, 40, and 80 simulated years after the onset of the ocean-forcing perturbation) for each basal rheology, with $m = 3$ and the bedrock profiles displayed in black and other ice-profile colors as in Fig. 2. Inset panel d), basal-friction-coefficient fields for the various basal rheologies (shown on a semi-log plot).

to flotation. Similar to the constant-rheology runs on these longer-wavelength beds, the net effect of shifting the mixed-bed rheology from more-nearly-viscous peaks to more-nearly-viscous stoss sides is still to delay retreat.

The stoss-lee friction field also increases stability for the shorter wavelength bed of Run Suite D' (Fig. 4), especially for higher bed exponents. The extra thickness over the troughs postpones upstream extension of the ice shelf beyond still-grounded areas on bathymetric highs, thereby delaying the characteristic stepped retreat. The grounding line still spends most of its time on the lee side of bumps, but less than it did in the D simulations. However, this decrease in stability is more than compensated by the extra time spent on the more-resistant stoss sides in the constant-rheology D' runs. This is not the case for mixed-rheology simulations. During the second half of the forcing period across closely-spaced bumps, localized basal drag drops to zero in the limit of more-rapid upstream ice-shelf extension, ultimately leading to a net decrease in outlet-glacier stability (cf. D and D' simulations).

5. Discussion

Prior modeling of TG forced by perturbations to the surface mass balance, basal mass balance, and basal conditions demonstrated that a viscous bed favors greater instability by localizing thinning near the grounding line, which is currently stabilized on a topographic ridge; the resulting retreat into the deep basin behind the ridge triggers MISI and ice-sheet collapse. In comparison, a more-nearly plastic bed is initially more stable because it limits localized thinning near the grounding line, instead spreading the thinning far inland (Parizek et al., 2013). This occurs because ice maintains force balance (Paterson, 1994), and reduced buttressing force from the ice shelf must be balanced by increased force from basal shear stress generated by higher basal velocity. Increased side drag could also contribute to restoring force balance, but the great width of TG– widening upglacier from ∼50 km to well over 100 km within 150 km of the current grounding zone– makes side drag less important, motivating the flowline simulations here. Fully resolved 3-d simulations of TG clearly would be of value. The study here is not intended to provide a full simulation of Thwaites, but to guide the field studies needed to allow such a simulation.

More-nearly plastic beds generate less additional stress for unit increase in velocity, instead transmitting velocity and stress increases inland. Once instability is triggered for a more-nearly plastic bed, however, the faster thinning far inland leads to more rapid retreat. Further extending prior results, the interplay of basal topography with basal rheology, including mixed-rheology beds, proves important to the pacing of retreat. Closer spacing of bathymetric ridges generally provides stability, up to a point. Placing additional drag on stoss sides and reducing drag on lee sides of ridges provides additional stability, except in the case of mixed-rheology and shorter-wavelength beds, where the specification of hard- versus soft-bedded regions leads to vastly different retreat characteristics. In addition, for mixed-rheology beds, extra basal shear stress is generated primarily over viscous zones, as more-plastic zones distribute stresses inland to the next viscous zone (Joughin et al., 2009). The enhanced internal stresses and localized thinning over the more-viscous zones then accelerate retreat when compared to uniformly effectively-plastic beds, thereby limiting some of the initial stability offered by effectively-plastic beds in most of our simulations.

5.1. Constant rheology

Effectively-plastic beds resulted in longer initial stability for all bedrock configurations tested. For example, after 40 years of forced retreat on the relatively long-wavelength bed shown in Fig. 2, the grounding line for the linear-viscous bed is approximately 5 km farther upstream than the effectively-plastic bed. Additionally, the mid-retreat profile of the linear-viscous bed is substantially thicker upstream and thinner near the grounding line than both of the higher-exponent beds. Similar patterns of retreat are observed across all other simulation types, consistent with previous modeling results (Parizek et al., 2013). Once triggered, though, retreat on more-nearly-plastic beds is faster, as the grounding line migrates into the already-thinned inland ice. This late-stage instability of plastic beds is especially evident on those beds we tested with shorter-wavelength topography. For example, the final grounding line on the $\lambda = 8$ km bed is farther upstream for the effectively-plastic basal rheology than for the weakly non-linear and linear-viscous beds (Fig. 3).

5.2. Mixed rheology

For the inclined-plane and long-wavelength beds, the behavior of the $m = 3 \leftrightarrow 8$ mixed-rheology simulations falls between those for constant-rheology $m = 3$ and $m = 8$ beds, suggesting that bounding the behavior of outlet glacier flow over mixed rheologies might be possible with appropriate single-rheology experiments. Behavior is more complex for shorter wavelengths, however.

For Run Suite D ($\lambda = 8$ km bed), the mixed-rheology with weakly non-linear peaks and effectively-plastic troughs is the most stable (Fig. 3). But, shifting the weak non-linearity to stoss sides and the effectively-plastic rheology to lee sides, with surface velocities matched to the Control Run for Run Suite D (Control with constant basal-friction coefficient), made the mixed-rheology bed the least stable. Keeping this geometric pattern but matching surface velocities to the Control Run of Run Suite D' (Control with sinusoidal basal-friction coefficient) made the run slightly more stable than the constant effectively-plastic bed (Fig. 4), similar to Run Suite B (Fig. 2). These differences further highlight the importance of data-constrained initializations and rheology specifications.

5.3. Basal topography

Threshold behavior is exhibited across bumpy beds, as grounding lines tend to jump back and then temporarily stabilize on basal highs (e.g., Wellner et al., 2006; Alley et al., 2007; Joughin et al., 2010; Parizek et al., 2010). This behavior is consistent across all basal rheologies tested, and becomes more pronounced with decreasing wavelength of bumps.

Reducing the topographic wavelength sufficiently (to 8 km for the linear viscous case and 10 km for the others) causes thinning sufficient to cause flotation inland of still-grounded regions, followed by expansion of the floating regions until they join, ungrounding from the bathymetric high. Not surprisingly, applying rapid oceanic melt rates to the inland ice-shelf extensions speeds retreat, an effect that becomes more important as the wavelength of the topography is reduced.

To further explore this behavior, we conducted additional sensitivity tests in which we inserted a 20-km zone of $\lambda = 2$ km wavelength bed, substantially reducing the stability of the outlet glacier across that zone. Such a short wavelength allows multiple inland extensions to form during retreat, thereby increasing the surface area of ice floating across these regions, and also leads to significant stress concentrations within the overlying grounded ice column. The higher basal melt rates over these floating regions drastically reduce the stability afforded by localized contact on neighboring bumps. Secondarily, the reduced ice viscosity due to higher localized stresses leads to higher shear-strain rates where grounded. Taken together, these cause rapid grounding-line retreat across the rough bed.

6. Conclusion

Thwaites Glacier (TG) in West Antarctica is thinning and retreating in response to warming of ocean water beneath its ice shelf. Retreat of the grounding zone of TG beyond some poorly known threshold could trigger sea-level rise in excess of 3 m (e.g., Pollard et al., 2015). Experiments with our flowline model configured to be similar to TG and forced by increased oceanic melting of its ice shelf show that outlet glacier (in)stability and retreat rate depend sensitively on numerous aspects of the environment. Rheology of the bed (more-nearly plastic or viscous, or mixed), topography, and the extent of ice-ocean interactions have unique yet coupled influences on ice-sheet dynamics.

A more-nearly linear-viscous bed localizes thinning near the grounding line, triggering retreat, whereas a more-nearly plastic bed minimizes thinning there by extending the influence farther inland. Once triggered, however, retreat on the plastic bed into the already-thinned ice is faster. Mixed-rheology beds, alternating between more-nearly viscous and plastic, exhibit intermediate behavior under some conditions but, surprisingly, can be more stable or more unstable under other conditions, with behavior depending critically on the length-scales of variability. Ultimately, the time-evolution of the surface is diagnostic of the flow law at the bed, providing an indirect observational method for discerning current bed properties and predicting future retreat.

The wavelength of basal topography exerts important controls on stability, and how the stability interacts with rheology, down to the shortest wavelengths we studied. Reducing the topographic wavelength from 10 km to 8 km, for example, resulted in outlet-glacier flow over an effectively-plastic bed transitioning from most stable to least stable under some conditions, and introduced upglacier ungrounding for the viscous rheology across all scenarios (a process that is initiated at wavelengths somewhat greater than 10 km for the higher-exponent beds). The rate of melting above such upglacier regions of ungrounding in turn strongly affects modeled TG stability.

Taken together, these results show the need for highly resolved (few-kilometer or less) measurements of basal topography, together with observational constraints on bed properties that capture their spatial heterogeneity. The retreat behavior of marine ice sheets depends sensitively on topography and rheology as well as lubrication. To properly capture future response of Thwaites Glacier to forcing, including possible ridge ungrounding and unstable collapse, 3-D modeling with a more complex treatment of bed rheology driven by improved field data will be required.

Acknowledgements

This research was supported by the U.S. National Science Foundation under grants ANT-0424589 (B.R.P., R.B.A.), AGS-1338832 (B.R.P., R.B.A.), PLR-1443190 (S.J.K., B.R.P.), NSF-NERC-OPP-1738934 (B.R.P., R.B.A., A.M.), and DGHZ55832 (N.H.), by NASA under grants NNX15AH84G (S.J.K., B.R.P., A.M.) and NNX16AM01G (N.H.), and by the Heising-Simons Foundation under grant 2018-0769 (B.R.P., R.B.A.). The authors would like to recognize the efforts of the Scientific Editor, Miaki Ishii, and the three anonymous referees. Their critical reviews were invaluable. Metadata will be submitted to the Antarctic Master Directory at USAP. Model output files are also available through the corresponding author upon request.

Appendix A. Supplementary material

Supplementary material related to this article can be found online at https://doi.org/10.1016/j.epsl.2019.03.026.

References

Alley, R.B., Anandakrishnan, S., Dupont, T.K., Parizek, B.R., Pollard, D., 2007. Effect of sedimentation on ice-sheet grounding-line stability. Science 315 (5820), 1838–1841. https://doi.org/10.1126/science.1138396.

Alley, R.B., Anandakrishnan, S., Christianson, K., Horgan, H.J., Muto, A., Parizek, B.R., Pollard, D., Walker, R.T., 2015. Oceanic forcing of ice-sheet retreat: West Antarctica and more. Annu. Rev. Earth Planet. Sci. 43, 7.1–7.25. https://doi.org/10.1146/annurev-earth-060614-105344.

Bamber, J.L., Riva, R.E.M., Vermeersen, B.L.A., LeBrocq, A.M., 2009. Reassessment of the potential sea-level rise from a collapse of the West Antarctic ice sheet. Science 324 (5929), 901–903. https://doi.org/10.1126/science.116935.

Bindschadler, R.A., et al., 2013. Ice-sheet model sensitivities to environmental forcing and their use in projecting future sea level (the SeaRISE project). J. Glaciol. 59 (214), 195–224. https://doi.org/10.3189/2013JoG12J125.

Christianson, K., Bushuk, M., Dutrieux, P., Parizek, B.R., Joughin, I., Alley, R.B., Shean, D.E., Abrahamesen, P., Anandakrishnan, S., Heywood, K.J., Kim, T.W., Lee, S.H., Nicholls, K., Stanton, T., Truffer, M., Webber, B., Jenkins, A., Jacobs, S., Bindschadler, R., Holland, D.M., 2016. Sensitivity of Pine Island Glacier to observed ocean forcing. Geophys. Res. Lett. 43. https://doi.org/10.1002/2016GL070500.

DeConto, R.M., Pollard, D.M., 2016. Contribution of Antarctica to past and future sea-level rise. Nature 531, 591–597.

Dupont, T.K., Alley, R.B., 2005. Assessment of the importance of ice-shelf buttressing to ice-sheet flow. Geophys. Res. Lett. 32, L04503. https://doi.org/10.1029/2004GL022024.

Dutrieux, P., De Rydt, J., Jenkins, A., Holland, P.R., Ha, H.K., Lee, S.H., Steig, E.J., Ding, Q., Abrahamsen, E.P., Schröder, M., 2014. Strong sensitivity of Pine Island ice-shelf melting to climatic variability. Science 343, 174–178. https://doi.org/10.1126/science.1244341.

Glen, J.W., 1955. The creep of polycrystalline ice. Proc. R. Soc. A, Math. Phys. Eng. Sci. 228, 519–538.

Goldberg, D., Holland, D.M., Schoof, C., 2009. Grounding line movement and ice shelf buttressing in marine ice sheets. J. Glaciol. 114 (F4). https://doi.org/10.1029/2008JF001227.

Golledge, N.R., Kowalewski, D.E., Naish, T.R., Levy, R.H., Fogwill, C.J., Gasson, E.G.W., 2015. The multi-millennial Antarctic commitment to future sea-level rise. Nature 526, 421–425. https://doi.org/10.1038/nature15706.

Harig, C., Simons, F.J., 2015. Accelerated West Antarctic ice mass loss continues to outpace East Antarctic gains. Earth Planet. Sci. Lett. 415, 134–141. https://doi.org/10.1016/j.epsl.2015.01.029.

Horgan, H.J., Alley, R.B., Christianson, K., Jacobel, R.W., Anandakrishnan, S., Muto, A., Beem, L.H., Siegfried, M.R., 2013. Estuaries beneath ice sheets. Geology 41 (11). https://doi.org/10.1130/G34654.1.

Hughes, T.J., 1981. The "weak underbelly" of the West Antarctic Ice Sheet. J. Glaciol. 27, 518–525.

Iken, A., 1981. The effect of subglacial water pressure on the sliding velocity of a glacier in an idealized numerical model. J. Glaciol. 27 (97), 407–422.

Jacobs, S.S., Hellmer, H.H., Jenkins, A., 1996. Antarctic ice sheet melting in the Southeast Pacific. Geophys. Res. Lett. 23, 957–960. https://doi.org/10.1029/96GL00723.

Jacobs, S.S., Jenkins, A., Giulivi, C.F., Dutrieux, P., 2011. Stronger ocean circulation and increased melting under Pine Island Glacier ice shelf. Nat. Geosci. 4, 519–523. https://doi.org/10.1038/ngeo1188.

Jenkins, A., Dutrieux, P., Jacobs, S.S., McPhail, S.D., Perrett, J.R., Webb, A.T., White, D., 2010. Observations beneath Pine Island Glacier in West Antarctica and implications for its retreat. Nat. Geosci. 3, 468–472. https://doi.org/10.1038/ngeo890.

Joughin, I., Howat, I.M., Fahnestock, M., Smith, B., Krabill, W., Alley, R.B., Stern, H., Truffer, M., 2008. Continued evolution of Jakobshavn Isbrae following its rapid speedup. J. Geophys. Res. 113, F04006. https://doi.org/10.1029/2008JF001023.

Joughin, I., Tulaczyk, S., Bamber, J.L., Blankenship, D., Holt, J.W., Scambos, T., Vaughan, D.G., 2009. Basal conditions for Pine Island and Thwaites Glacier, West Antarctica, determined using satellite and airborne data. J. Glaciol. 55 (190), 245–257. https://doi.org/10.3189/002214309788608705.

Joughin, I., Smith, B.E., Holland, D.M., 2010. Sensitivity of 21st century sea level to ocean-induced thinning of Pine Island Glacier, Antarctica. Geophys. Res. Lett. 37, L20502. https://doi.org/10.1029/2010GL044819.

Joughin, I., Smith, B.E., Medley, B., 2014. Marine ice sheet collapse potentially under way for the Thwaites Glacier basin, West Antartica. Science 344, 735–738. https://doi.org/10.1126/science.1249055.

Mercer, J.H., 1968. Antarctic Ice and Sangamon Sea Level. IAHS Spec. Publ., vol. 179, pp. 217–225.

Mouginot, J., Rignot, E., Scheuchl, B., 2014. Sustained increase in ice discharge from the Amundsen Sea Embayment, West Antarctica, from 1973 to 2013. Geophys. Res. Lett. 41 (5), 1576–1584. https://doi.org/10.1002/2013GL059069.

Muto, A., Anandakrishnan, S., Alley, R.B., Horgan, H.J., Parizek, B.R., Koellner, S., Christianson, K., Holschuh, N., 2019. Relating bed character and subglacial morphology using seismic data from Thwaites Glacier, West Antarctica. Earth Planet. Sci. Lett. 507, 199–206. https://doi.org/10.1016/j.epsl.2018.12.008.

Parizek, B.R., Alley, R.B., Dupont, T.K., Walker, R.T., Anandakrishnan, S., 2010. Effect of orbital-scale climate cycling and meltwater drainage on ice sheet grounding line migration. J. Geophys. Res. 115, F01011. https://doi.org/10.1029/2009JF001325.

Parizek, B.R., Christianson, K., Anandakrishnan, S., Alley, R.B., Walker, R.T., Edwards, R.A., Wolfe, D.S., Bertini, G.T., Rinhart, S.K., Bindschadler, R.A., Nowicki, S.M.J., 2013. Dynamic (in)stability of Thwaites Glacier, West Antarctica. J. Geophys. Res., Earth Surf. 118. https://doi.org/10.1002/jgrf.20044.

Paterson, W.S.B., 1994. The Physics of Glaciers, third ed. Pergamon, New York. 481 pp.

Payne, A.J., Viele, A., Shepherd, A., Wingham, D.J., Rignot, E., 2004. Recent dramatic thinning of largest West Antarctic ice stream triggered by oceans. Geophys. Res. Lett. 31, L23401. https://doi.org/10.1029/2004GL021284.

Pfeffer, W.T., Harper, J.T., Neel, S.O., 2008. Kinematic constraints on glacier contributions to 21st-century sea-level rise. Science 321, 1340–1343. https://doi.org/10.1126/science.1159099.

Pollard, D., DeConto, R.M., Alley, R.B., 2015. Potential Antarctic Ice Sheet retreat driven by hydrofracturing and ice cliff failure. Earth Planet. Sci. Lett. 412, 112–121.

Pritchard, H.D., Ligtenberg, S.R.M., Fricker, H.A., Vaughan, D.G., van den Broeke, M.R., Padman, L., 2012. Antarctic ice-sheet loss driven by basal melting of ice shelves. Nature 484, 502–504. https://doi.org/10.1083/nature10968.

Rathbun, A.P., Marone, C., Alley, R.B., Anandakrishnan, S., 2008. Laboratory study of the frictional rheology of sheared till. J. Geophys. Res. 113, F02020. https://doi.org/10.1029/2007JF000815.

Rignot, E., 1998. Fast recession of a West Antarctic Glacier. Science 281, 549–551.

Rignot, E., Mouginot, J., Morlighem, M., Seroussi, H., Scheuchl, B., 2014. Widespread, rapid grounding line retreat of Pine Island, Thwaites, Smith, and Kohler glaciers, West Antarctica, from 1992 to 2011. Geophys. Res. Lett. 41, 3502–3509. https://doi.org/10.1002/2014GL060140.

Ritz, C., Edwards, T.L., Durand, G., Payne, A.J., Peyaud, V., Hindmarsh, R.C.A., 2015. Potential sea-level rise from Antarctic ice-sheet instability constrained by observations. Nature 528 (7580), 115–118.

Schoof, C., 2005. The effect of cavitation on glacier sliding. Proc. R. Soc. A, Math. Phys. Eng. Sci. 461 (2055), 609–627. https://doi.org/10.1098/rspa.2004.1350.

Schoof, C., 2007. Ice sheet grounding line dynamics: steady states, stability, and hysteresis. J. Geophys. Res. 112, F03S28.

Schroeder, D.M., Blankenship, D.D., Young, D.A., Witus, A.E., Anderson, J.B., 2014. Airborne radar sounding evidence for deformable sediments and outcropping bedrock beneath Thwaites Glacier, West Antarctica. Geophys. Res. Lett. 41 (20), 7200–7208. https://doi.org/10.1002/2014GL061634.

Shean, D.E., Joughin, I.R., Dutrieux, P., Smith, B.E., Berthier, E., 2018. Ice shelf basal melt rates from a high-resolution DEM record for Pine Island Glacier, Antarctica. Cryosphere Discuss. https://doi.org/10.5194/tc-2018-209. In review.

Stocker, T.F., Qin, D., Plattner, G.-K., Tignor, M., Allen, S.K., Boschung, J., Nauels, A., Xia, Y., Bex, V., Midgley, P.M. (Eds.), 2013. Climate Change 2013: The Physical Science Basis. Contribution of Working Group I to the Fifth Assessment Report of the Intergovernmental Panel on Climate Change. Cambridge University Press, Cambridge, United Kingdom, New York, NY, USA. 1535 pp.

Tulaczyk, S., Kamb, W.B., Engelhardt, H.F., 2000. Basal mechanisms of Ice Stream B, West Antarctica. 2. Undrained plastic bed model. J. Geophys. Res. B 105 (1), 483–494.

Walker, R.T., Parizek, B.R., Alley, R.B., Brunt, K.M., Anandakrishnan, S., 2014. Ice-shelf flexure and tidal forcing of Bindschadler Ice Stream, West Antarctica. Earth Planet. Sci. Lett. 395, 184–193. https://doi.org/10.1016/j.epsl.2014.03.049.

Weertman, J., 1957. On the sliding of glaciers. J. Glaciol. 3 (21), 33–38.

Weertman, J., 1974. Stability of the junction of an ice sheet and an ice shelf. J. Glaciol. 13 (67), 3–11.

Wellner, J.S., Heroy, D.C., Anderson, J.B., 2006. The death mask of the Antarctic ice sheet: comparison of glacial geomorphic features across the continental shelf. Geomorphology 75, 157–171.